

1 **On the origin of seismic anisotropy in the shallow crust**
2 **of the Northern Volcanic Zone, Iceland**

3 **C. A. Bacon¹, J. Johnson², R. S. White¹, N. Rawlinson¹**

4 ¹Department of Earth Sciences, University of Cambridge, UK

5 ²School of Environmental Sciences, University of East Anglia, UK

6 **Key Points:**

- 7 • Anisotropy is caused by fracturing of brittle crust to a depth of 3–4 km.
8 • Orientation of the fast axis of anisotropy is rift parallel, and hence controlled by
9 regional stresses.
10 • Disruption of anisotropy pattern around Askja volcano likely caused by magmatic
11 intrusion and solidification.

Corresponding author: C. A. Bacon, conor.bacon@cantab.net

Abstract

The Icelandic crust is a product of its unique tectonic setting, where the interaction of an ascending mantle plume and the mid-Atlantic Ridge has caused elevated mantle melting, which has accreted and cooled in the crust to form an oceanic plateau. Here, we investigate the strength, orientation and distribution of seismic anisotropy in the upper crust of the Northern Volcanic Zone using local earthquake shear-wave splitting, with a view to understanding how the contemporary stress field may influence sub-wavelength structure and processes. This is achieved using a dataset comprising >50,000 earthquakes located in the top 10 km of the crust, recorded by up to 70 stations over a 9 year period. We find that anisotropy is largely confined to the top 3–4 km of the crust, with an average delay time of $0.10 \pm 0.08s$, and an average orientation of the fast axis of anisotropy of $N15^\circ \pm 33^\circ E$, which closely matches the spreading direction of the Eurasian and North American plates ($\sim N16^\circ E$). These results are consistent with the presence of rift-parallel cracks that gradually close with depth, the preferential opening of which is controlled by the regional stress field. Lateral variations in the strength of shear wave anisotropy reveal that regions with the highest concentrations of earthquakes have the highest SWA values ($\sim 10\%$), which reflects the presence of significant brittle deformation. Disruption of the orientation of the fast axis of anisotropy around Askja volcano can be related to local stress changes caused by underlying magmatic processes.

Plain Language Summary

Iceland is well known for its earthquakes and volcanoes, which have helped to produce an awe-inspiring primordial landscape over the last 20 million years or so. The emergence of Iceland in the North Atlantic ocean can be attributed to the interaction of the mid-Atlantic Ridge, where new oceanic crust is formed between the North American and Eurasian plates, and a rising conduit of hot mantle from deep in the Earth, known as a mantle plume. The confluence of these two phenomenon has produced excessive melting of mantle rocks, which has accreted and cooled to form the Icelandic crust. In this study, we investigate how extensional stresses related to the divergence of the two tectonic plates has influenced the upper 3–4 km of the crust in the Northern Volcanic Zone in the deep interior of Iceland. To do so, we exploit information contained in recordings of earthquakes from the neighbourhood of Askja volcano, which suggests that rift parallel cracks that gradually close with depth permeate the upper crust. This relationship between the regional stress field associated with rifting and brittle deformation in the uppermost crust breaks down around Askja volcano itself, where magmatic processes likely cause local changes in stress field.

1 Introduction

Iceland lies in the North Atlantic, at the confluence of the divergent plate boundary (defined by the mid-Atlantic Ridge) between the Eurasian and North American plates, and the Iceland plume (White & McKenzie, 1995). Through a combination of increased melt volumes (MacLennan et al., 2001) and dynamic support from the plume, Iceland has emerged from beneath the North Atlantic and steadily grown over the last 20 million years. The resultant oceanic crust is unusually thick, reaching up to 40 km (Allen, 2002; Darbyshire et al., 2000) beneath the main glacier, Vatnajökull. On land, the mid-Atlantic Ridge is expressed as a collection of en-*é*chelon axial rift systems, each typically comprising a central volcano and an elongated fissure swarm (Einarsson, 1991), and formally classified based on the surface fractures, faults and geochemistry of the erupted products. This neo-volcanic zone is broadly divided into three significant segments: the Western, Eastern, and Northern Volcanic Zones (WVZ, EVZ, and NVZ, respectively —Figure 1a). The Northern and Eastern zones have been offset by over 100 km from the mid-Atlantic Ridge by a series of eastward ridge jumps around 8–8.5 Ma (Garcia et al., 2003). The NVZ is subdivided into five distinct, mature volcanic systems, namely: Kverkfjöll, Askja, Fremrinámur, Krafla, and Þeistareykir. It is within these volcanic rift zones that plate spreading is accommodated through faulting and episodic accretion of new crust in volcanic intrusions and eruptions (e.g. Sigmundsson et al., 2014).

Askja is a large, active central volcano located at the southern end of the NVZ (see Figure 1). A complex, nested sequence of at least three caldera, spanning 20 km, constitutes the main volcanic edifice, which is composed primarily of hyaloclastite and pillow lavas erupted during the last glacial maximum. The last eruption of Askja was in 1961, when a 2 km-long fissure opened up, with lava breaching the eastern side of the main caldera wall. Surface mapping around Askja has revealed a complex pattern of both caldera-concentric and rift-parallel features (Graettinger et al., 2019; Hjartardóttir et al., 2016).

Deformation around Askja has been monitored since 1961, at first with a tilt line within the caldera (Sturkell et al., 2006; Tryggvason, 1989), but more recently using satellite-based GPS and InSAR measurements (de Zeeuw-van Dalssen et al., 2012; Pagli et al., 2006; Sturkell et al., 2006). The long term trend since 1961 is one of deflation, albeit at a decaying rate. Forward modeling of the geodetic observations has led to the possible discovery of a shallow (3.5 km), Mogi-type source beneath the Askja caldera that best fits the observed deflation, though most studies have assumed an isotropic, elastic half-space, which may be inappropriate around Askja (Drouin et al., 2017; Heimisson & Segall,

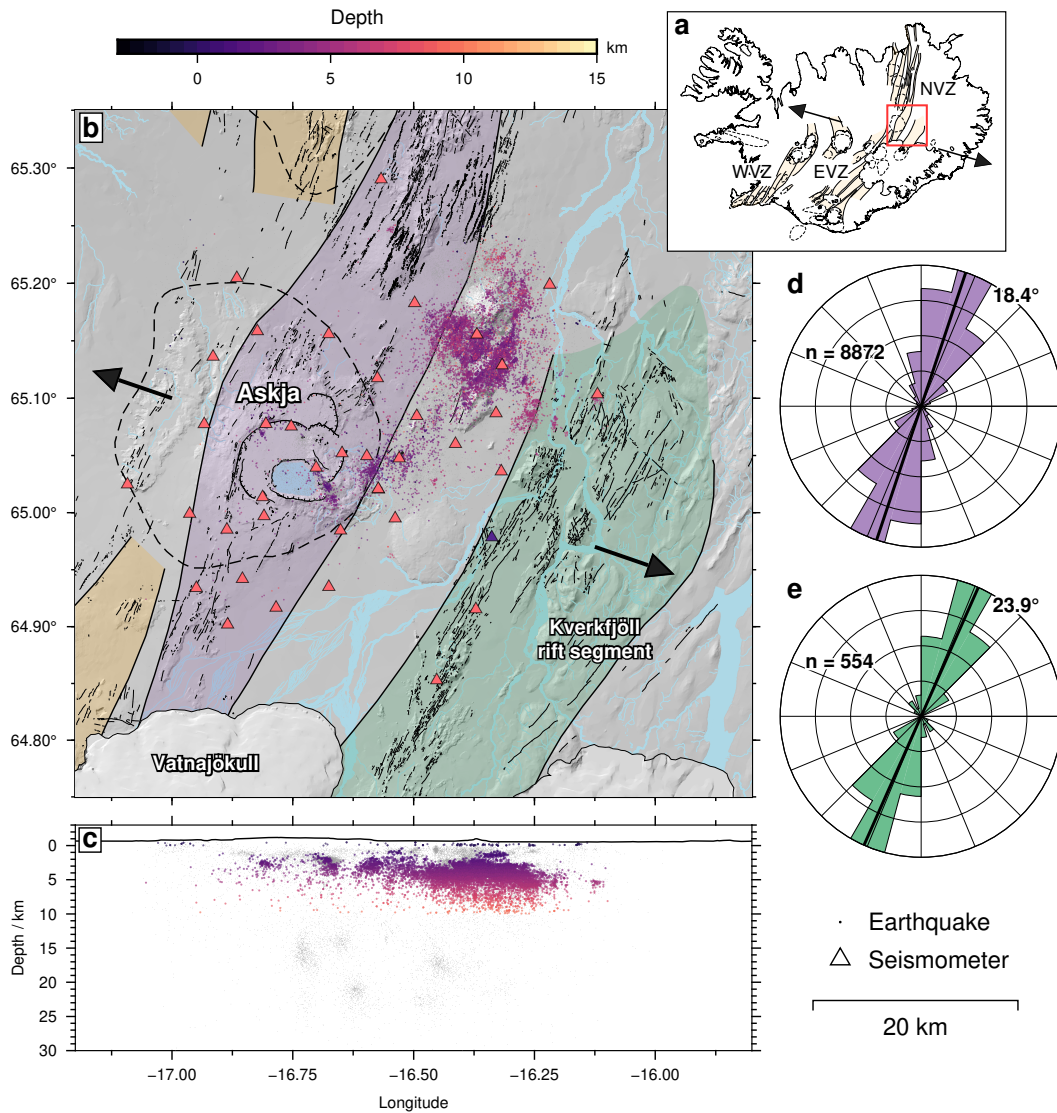


Figure 1. (a) Overview of Iceland with the major glaciers outlined. The orange bands delineate the en-echelon fissure swarms that characterise the on-land expression of the northern mid-Atlantic Ridge. The study region shown in panel (b) is outlined in red. (b) Shaded digital elevation map for the region around Askja volcano. Red triangles are seismic stations operated by the University of Cambridge used in this study. The purple triangle is the Icelandic Meteorological Office station, MKO. The entire earthquake catalog of Greenfield et al. (2018) is shown as grey dots, with those colored by hypocentral depth representing earthquakes used in this study. Two fissure swarms are highlighted: Askja's (purple) and Kverkfjöll's (green). The dashed line delineates the region associated with the Askja central volcano. The arrows show the regional direction of plate spreading, striking at $N106^{\circ}E$ (c) An east-west section showing the earthquake catalog locations. (d) and (e) are polar histograms of surface features (fractures, fissures, faults) mapped by Hjartardóttir et al. (2016) for the Askja and Kverkfjöll fissure swarms, respectively, with average strikes of 18.4° and 23.9° shown by the black bars. n is the number of features in each sample.

2020). For instance, rheological models based on a visco-elastic ridge appear to be key in the interpretation of geodetic data (Pedersen et al., 2009).

Large systems of fissures and faults are widespread across the rift segments associated with Askja and another central volcano, Kverkfjöll, situated to the southeast (see Figure 1). A network of cross-cutting faults are thought to accommodate the strain due to relative extension between these two segments (Green et al., 2014), though elsewhere the areas between the rift segments are relatively aseismic, suggesting they experience lower stress. These faults are responsible for the bulk of the seismic activity in the southern NVZ. This seismicity tends to occur in swarms (where the earthquakes are clustered in both space and time), located primarily above the well-mapped brittle-ductile transition at around 8 km depth (Soosalu et al., 2010). There is also significant seismic activity in the Öskjuvatn caldera, which lies within Askja, associated with the migration of geothermally heated fluid, as well as a number of deep clusters of earthquakes thought to be associated with the migration of melt between layered sills (Greenfield et al., 2018).

Seismic anisotropy, the directional dependence of seismic wave-speed, has been observed in the crust across a range of environments (Boness & Zoback, 2006; Johnson et al., 2011; Illsley-Kemp et al., 2018). The nature of anisotropy can, broadly, be described as either effective, i.e. a long-wavelength, bulk property of an otherwise heterogeneous medium, or intrinsic anisotropy, arising from the anisotropic elastic structure at the crystal lattice level. The latter, commonly known as Lattice Preferred Orientation (LPO), is often invoked to explain observations of anisotropy in the upper mantle, which is predominantly composed of the anisotropic minerals olivine and orthopyroxene. When deformed under strain, these minerals preferentially align, giving rise to anisotropy on a macroscopic scale. It has also been proposed as a mechanism to explain observations of Love and Rayleigh wave anisotropy in the lower crust of Iceland from ambient noise analysis (Volk et al., 2021). However, it is effective anisotropy that is typically invoked as the primary mechanism behind seismic anisotropy in the shallow, brittle crust. Here, mechanisms are typically related to either stress, through preferential closure of micro-cracks (or Extensive Dilatancy Anisotropy, EDA Crampin, 1994), oriented melt pockets (OMP; Holtzman et al., 2003; Keir et al., 2005; Bastow et al., 2010), structure, such as repeating isotropic layers (Backus, 1962) or damage zones around faults (Boness & Zoback, 2006). We seek here to determine the mechanism, or mechanisms, responsible for generating seismic anisotropy in the crust around Askja in order to better understand the state and structure of nascent crust formed at a mid-ocean ridge. Mapping and understanding this regional anisotropy is key to studying how the crust responds to transient stress changes, such as those induced by volcanic intrusions and eruptions.

118 Shear-wave splitting is one of the most unambiguous indicators of seismic anisotropy.
119 When a linearly polarised shear wave impinges on an anisotropic medium, it is partitioned
120 into two quasi-S waves, which propagate with different wavespeeds. The polarisation of
121 these two waves, commonly called ‘fast’ (denoted ϕ hereafter) and ‘slow’, is determined
122 by the symmetry and orientation of the anisotropic elastic tensor. A time lag, δt , accrues
123 between the polarised waves as they propagate through the region, with the final inte-
124 grated value proportional to both the path length and the strength of anisotropy. Sig-
125 nificant work has been done to establish methods that can distinguish between struc-
126 tural and stress-induced anisotropy (Johnson et al., 2011; Boness & Zoback, 2006), since
127 being able to do so is critical for the application of time-series analysis to shear-wave split-
128 ting observations as a means of monitoring the evolution of the stress field in volcanic
129 environments in response to seasonal signals, long-term temporal signals (such as defla-
130 tion and inflation), and stress transients resulting from volcanic processes such as caldera
131 collapse and dike intrusions. In both structural and stress-induced anisotropy, the frac-
132 ture density and fracture aspect ratio are among some of the dominant controls on the
133 amount of splitting accumulated along the raypath.

134 Here we perform local earthquake shear-wave splitting analysis in the neighbour-
135 hood of the volcano Askja for the first time, in order to relate observed anisotropy to the
136 underlying processes responsible for the accretion of new crust at a mid-ocean ridge and
137 the development of associated volcanic systems. The results provide a new perspective
138 on a region that is already well studied using complementary geophysical methods (Sturkell
139 et al., 2006; de Zeeuw-van Dalssen et al., 2012; Greenfield et al., 2016, 2018; Drouin et
140 al., 2017).

141 **2 Data and Methods**

142 **2.1 Data**

143 We use continuous seismic data recorded by a network of 3-component seismometers op-
144 erated by the University of Cambridge since 2008, with additional data from one instru-
145 ment operated by the Icelandic Meteorological Office (MKO, denoted by the purple tri-
146 angle in Figure 1). Over time, the network has consisted of between 30 and 70 broad-
147 band instruments, primarily Gralp 6TDs (30 s corner frequency). All data used in this
148 study were recorded using Gralp 6TDs. For the shear-wave splitting analysis, we use
149 the earthquake catalog of Greenfield et al. (2018) which spans 2009–2015, updated (us-
150 ing the same methodology outlined in their paper) to include data recorded between 2015
151 and 2018 (Winder et al., 2018). These earthquakes were detected and located using the
152 automatic Coalescence Microseismic Mapping algorithm (CMM: Drew et al., 2013). The

153 details of pre-processing applied to the data to generate this catalog is available in Greenfield
 154 et al. (2018). The CMM algorithm produces automatic arrival time picks for P- and S-
 155 phases that were used, along with some manually picked phase arrivals, to relocate the
 156 events using NonLinLoc (Lomax et al., 2000). The final catalog consists of 58,143 indi-
 157 vidual earthquakes spanning a local magnitude range of -0.6–4.0, with a magnitude of
 158 completeness of ≈ 1 .

159 The majority of earthquakes (52,141, or 89.7%) occur in the brittle, upper 7 km
 160 of crust, generated primarily by a network of cross-cutting conjugate strike-slip faults
 161 oriented N-S and SW-NE, located to the northeast of Askja volcano and to the south
 162 of Herðubreið, a tuya formed during the last glacial period (Figure 1a). These faults ac-
 163 commodate tectonic stresses that are concentrated by the relative spreading between the
 164 Askja and Kverkfjöll rift segments. The remaining shallow seismicity is related to geother-
 165 mal processes at Askja volcano. The depths of these shallow events are well-distributed
 166 throughout the brittle crust. The final 10.3% (6,002) of events in the catalog occur in
 167 pockets at depths between 7 and 25 km in the typically aseismic lower, ductile crust. These
 168 are thought to be associated with magmatic processes (Greenfield et al., 2018; Martens
 169 & White, 2013). We limit our analyses to splitting observed from earthquakes originat-
 170 ing in the upper 10 km of crust in order to specifically focus on anisotropy in the shal-
 171 low crust. Finally, we exclude any events that occurred between August 2014 and Febru-
 172 ary 2015 in order to remove the possible effect of stress transients related to the 2014–
 173 15 eruption of Bárðarbunga. Figure 1 illustrates the spatial distribution of earthquakes
 174 and seismic stations between 2009 and 2018 that have been used in this study.

175 2.2 Shear-wave splitting

176 We measure the shear-wave splitting parameters $(\phi, \delta t)$ using the Multiple Filter
 177 Automatic Splitting Technique package (MFAST version 2.2 Savage et al., 2010; Teanby
 178 et al., 2004), which uses the eigenvalue minimisation algorithm of Silver and Chan (1991).
 179 Figure 2 illustrates the process for a good quality event; further examples can be found
 180 in the Supplementary information (see Figures S1-4). Unlike other methods, this does
 181 not require any knowledge of the initial polarisation, though at the cost of being more
 182 prone to cycle skipping. A grid search over δt and ϕ is used to find the pair of values that
 183 best remove the observed splitting, determined by measuring the linearity of particle mo-
 184 tion on the horizontal components within a window around the S-phase arrival. This is
 185 further automated by trialing multiple windows and using cluster analysis to identify sta-
 186 ble results. Errors for individual measurements are calculated by conducting an F-test
 187 and finding the 95% confidence interval on the optimal $(\delta t, \phi)$ (Walsh et al., 2013). Each

188 measurement is automatically graded based on the distribution of clusters and the tight-
 189 ness of the misfit contours from the grid search (Savage et al., 2010). Also, MFAST tri-
 190 als a suite of filters over the S-phase pick in order to determine the filter that most ef-
 191 fectively boosts the signal-to-noise ratio. Table S1 in the supporting information pro-
 192 vides an overview of the final parameters used for MFAST.

193 We limit our analyses to the subset of measurements that satisfy the following cri-
 194 teria: a signal-to-noise ratio (as defined in Savage et al., 2010) greater than 4; clusters
 195 graded ‘‘ACI’’ (a measure of the number of clusters identified and how tight they are);
 196 errors in $\phi < 10^\circ$ in order to mitigate erroneous observations resulting from cycle skip-
 197 ping; values of $\delta t < 0.48s$, equal to 0.8 times the maximum delay time of the search;
 198 and errors in $\delta t < 0.05s$ as an additional filter against ‘null’ measurements and poorly
 199 constrained results. A null measurement can occur when there is no anisotropy in the
 200 plane of the shear wave particle motion, or when the source polarisation of the shear wave
 201 is along the fast or slow orientation of the medium. Source polarisations are determined
 202 from the uncorrected horizontal particle motion. Measurements of ϕ within 20° of the
 203 source polarisation are considered too ambiguous in that they cannot be definitively dis-
 204 tinguished from nulls. After applying these criteria, we are left with over 100,000 mea-
 205 surements of shear-wave splitting. Finally, we further remove measurements for which
 206 the angle of incidence of the shear wave at the surface falls outside the shear-wave win-
 207 dow (Nuttli, 1961). This window, defined by $\sin^{-1}(V_s/V_p)$, is the angle to the vertical
 208 at which there will be non-negligible interactions with the free surface that would alter
 209 the phase and amplitude information on the horizontal components (Crampin, 1984).
 210 A V_p/V_s ratio of 1.78 corresponds to a shear-wave window of $\sim 34^\circ$ from the vertical.
 211 However, volcanic environments typically exhibit very low velocities in the topmost lay-
 212 ers (Lesage et al., 2018), which will cause significant deflection of the ray towards the
 213 vertical. Therefore, we limit our analysis to event-station pairs with a straight-line angle-
 214 of-incidence at the surface of $< 50^\circ$. This leaves over 16,000 high-quality measurements
 215 of shear-wave splitting.

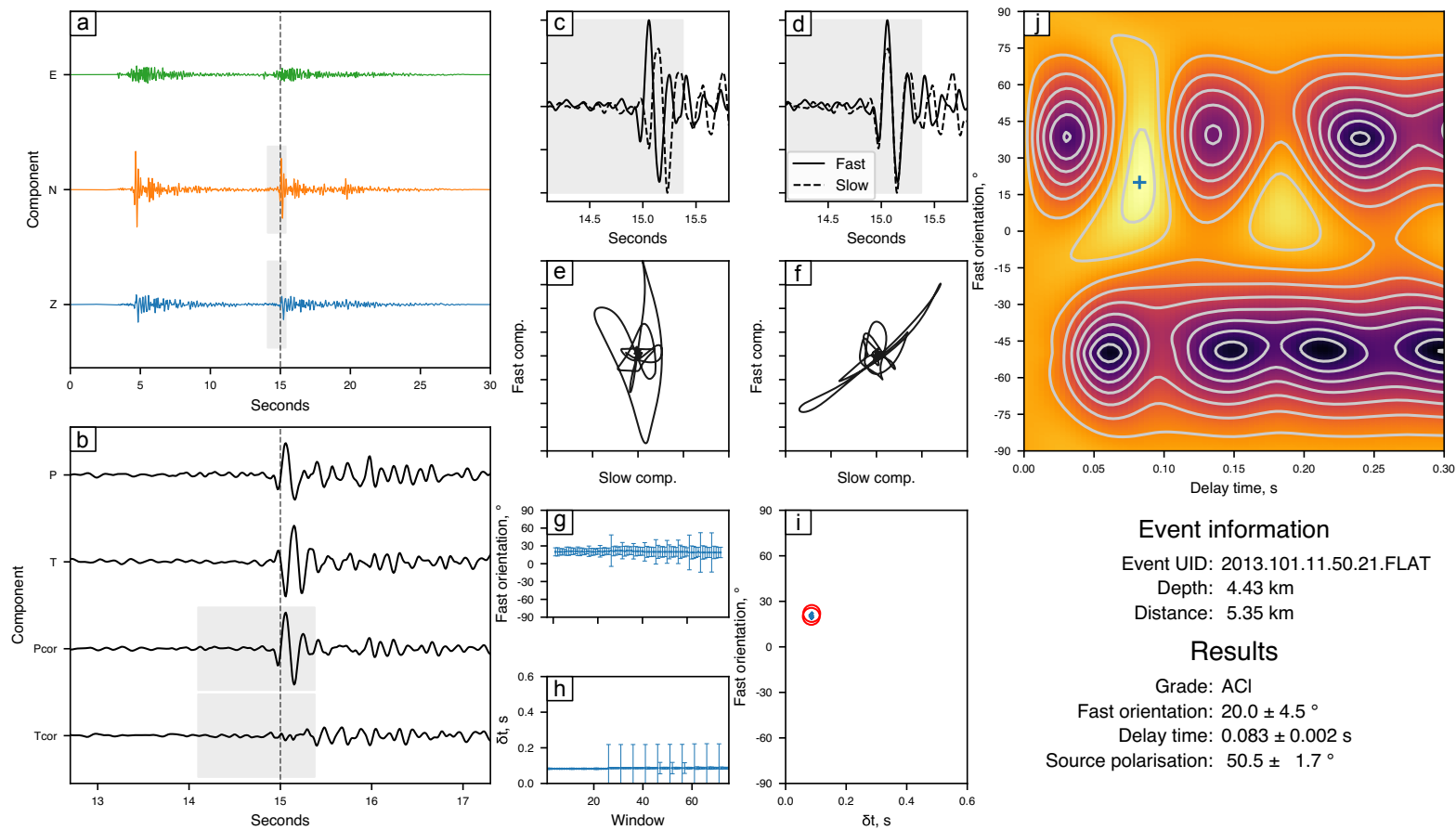


Figure 2. An example of a good splitting measurement. (a) shows the raw data for the East (green), North (orange), and Vertical (blue) components. (b) shows a zoom in around the S phase arrival rotated onto the nominal ‘radial’ (P) and ‘transverse’ (T) axes before and after correction for splitting. (c) and (d) show the phase arrivals rotated onto the ‘fast’ and ‘slow’ axes before and after correction, with (e) and (f) showing the corresponding particle motion. There is a clear linearisation of the particle motion of the horizontal components and removal of energy from the transverse component. Panels (g) - (i) show the results of the multiple window trials and the cluster analysis. Finally, (j) shows the resultant grid of the minimised eigenvalue. The blue cross denotes the optimal $(\delta t, \phi)$ pair.

216

2.3 Shear Wave Anisotropy

The delay time is an integrated measure of the strength of anisotropy along the ray-path, making it unsuitable for direct comparison between different event-station pairs. Instead, the observed delay times are converted to shear wave anisotropy (SWA: Thomas & Kendall, 2002), which is a measure of the strength of anisotropy as defined by the fractional perturbation, a , from the average shear wave speed, \bar{v} :

$$\begin{aligned}\delta t = t_{slow} - t_{fast} &= \frac{d}{v - \frac{1}{2}av} - \frac{d}{v + \frac{1}{2}av} \\ \Rightarrow a &= \frac{-2d}{\delta t \bar{v}} \pm \sqrt{4 + \left(\frac{2d}{\delta t \bar{v}}\right)^2}\end{aligned}\tag{1}$$

217

218

219

220

221

222

223

224

225

226

227

where t_{slow} and t_{fast} are the slow and fast traveltimes, respectively. SWA is normalised against the path length, d , of the ray, therefore representing a more appropriate metric to compare between individual observations. We assume straight-line raypaths and use an optimal 1-D velocity model determined by inverting microseismic arrival times (Mitchell et al., 2013). Nowacki et al. (2018) demonstrates that the errors introduced by the straight-line raypath assumption is negligible for shallow events, for which the raypaths do not deviate far from a straight line, with up to around 1% overestimation in SWA for the deepest events. Additionally, they show that the uncertainty in SWA arising from inaccuracy in the velocity model is estimated to be less than 1% from bootstrap modeling. Given the similarities between the regions of study (Iceland and the Afar), we believe that this uncertainty analysis remains appropriate.

228

3 Results

229

3.1 Regional averages

230

3.1.1 Delay times

231

232

233

234

235

236

237

238

239

240

241

From the entire catalog of shear-wave splitting measurements, we recover an average delay time of $\delta t = 0.10 \pm 0.08$ s. This value is consistent with similar datasets, e.g. ~ 0.2 s around Soufrière Hills volcano, Montserrat (Baird et al., 2015); 0.1–0.2 s in the Western Volcanic Zone, Iceland (Menke et al., 1994); and 0.11 ± 0.06 s around Aluto volcano, Ethiopia (Nowacki et al., 2018). We find the distribution of delay time observations to be sufficiently normal, justifying the extraction of a regional 1-D depth profile as the central tendency of the data via the application of a rolling arithmetic mean (Figure 3). We use a 1.5 km rolling window, spaced every 0.75 km, which is controlled by the uncertainty in hypocentral depth for shallow events. We observe a constant delay time at depths > 3 km. Between 3 km depth and the surface, the delay time begins to trend towards 0, which is consistent with a finite-thickness anisotropic layer in the very

242 shallow crust, a common observation across volcanic environments (Johnson et al., 2011;
 243 Menke et al., 1994; Nowacki et al., 2018). This does not preclude structural control on
 244 anisotropy, but it is a key requirement for stress-induced anisotropy due to the prefer-
 245 ential closure of microcracks. In oceanic-type crust, most pore space has been closed by
 246 lithostatic pressure at around 4–5 km below the surface (Christensen, 1984). The rela-
 247 tionship between crustal porosity and depth can be expressed as the exponential func-
 248 tion (e.g. Athy, 1930; Audet & McConnell, 1992):

$$\Phi(r) = \Phi_1 \exp\left(\frac{-c * P(r)}{P_c}\right) \quad (2)$$

249 where c is a constant (~ 6.15), Φ_1 is the surface porosity, $P(r)$ is the lithostatic over-
 250 burden pressure ($= \rho(r)gd$, where ρ is the density, g is the acceleration due to gravity,
 251 and d is the depth), and P_c is the characteristic closing pressure of the material (Han
 252 et al., 2014). We perform a simple fit of a similar exponential function to the depth pro-
 253 file, shown in Figure 3, which suggests that the 1-D behaviour of the delay time is con-
 254 sistent with the presence of crustal cracks that gradually close with increasing depth.

255 **3.1.2 Fast axis orientation**

256 We observe an average orientation of $\phi \sim \text{N}15^\circ\text{E} \pm 33^\circ$ for the fast axis of anisotropy,
 257 though we recommend caution in drawing too much from the exact value of, and the un-
 258 certainty on, this measure as the circular statistics used are only appropriate if the ob-
 259 servations are drawn from a unimodal distribution. Small variations in fast polarizations
 260 across the region, such as those expected in response to e.g. a rotation in the stress field,
 261 may be contributing to the large spread in observed ϕ values. The average orientation
 262 correlates well with the normal to the plate-spreading direction, as shown in Figure 4,
 263 which is consistent with observations made at other spreading centres, such as the north-
 264 ern Main Ethiopian Rift (Keir et al., 2005). Exactly how the orientation of the fast axis
 265 of anisotropy varies across the region is investigated further in Section 3.2.2.

266 **3.2 Lateral variations in observed anisotropy**

267 **3.2.1 Shear wave anisotropy**

268 Measurements of delay time are converted to SWA using equation 1, as described
 269 in section 2.3. We constrain the shallow anisotropic layer to be entirely above ~ 3 km
 270 b.s.l., inferred from the constant delay time below this depth observed in the 1-D pro-
 271 file (Figure 3). Assuming that the mechanism generating seismic anisotropy is aligned
 272 fractures in the shallow crust, this value is consistent with measures of fracture density

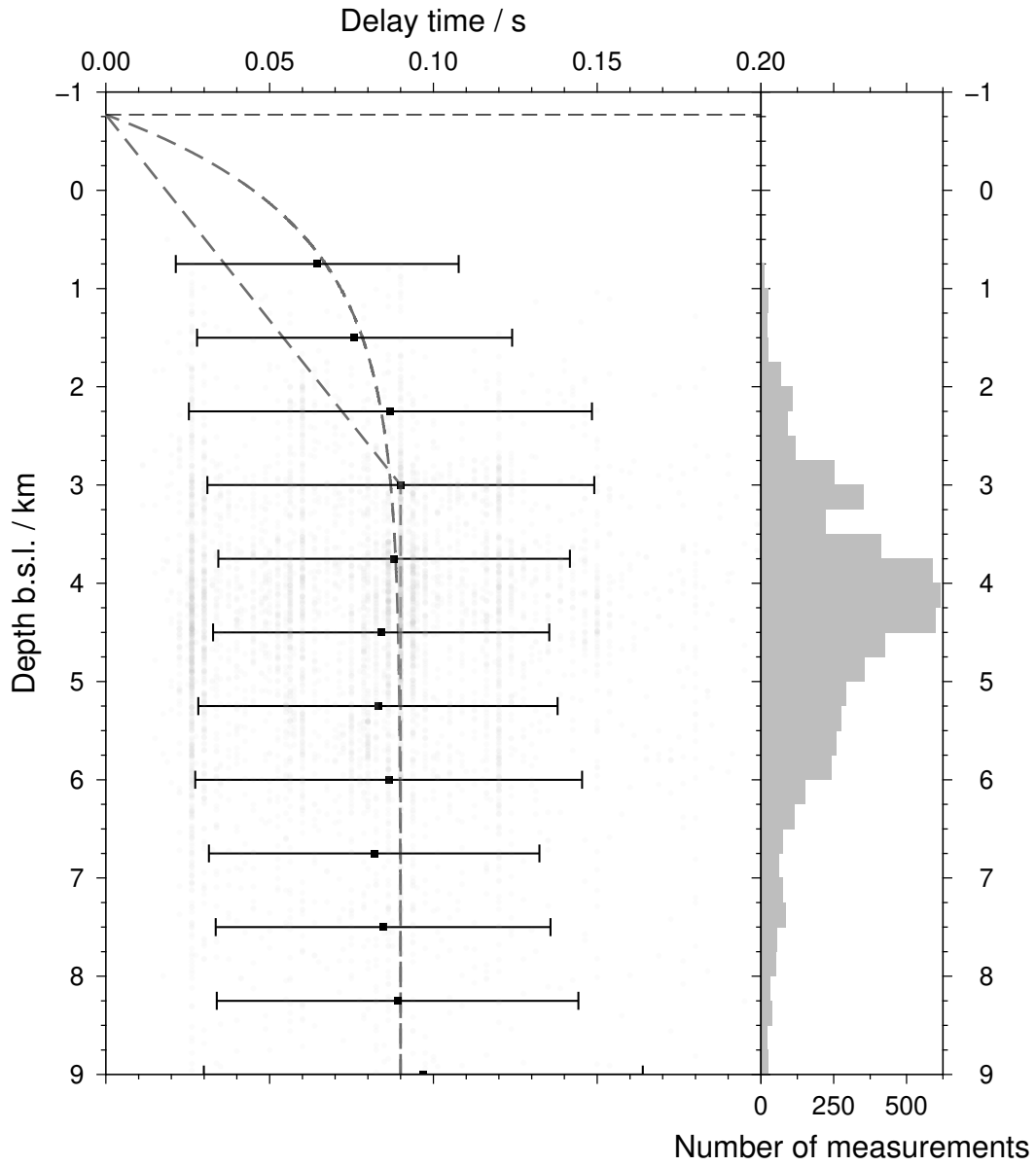


Figure 3. 1-D depth profile of delay time from a 1.5 km wide rolling window, spaced every 0.75 km. The dashed lines show the expected trends for a finite-thickness anisotropic layer down to 3 km depth with a strength of 3.4% and an exponential model based on the reduction of porosity as a function of depth. Black squares show the measured arithmetic means for each bin, with the associated one standard deviation of uncertainty shown by the error bars.

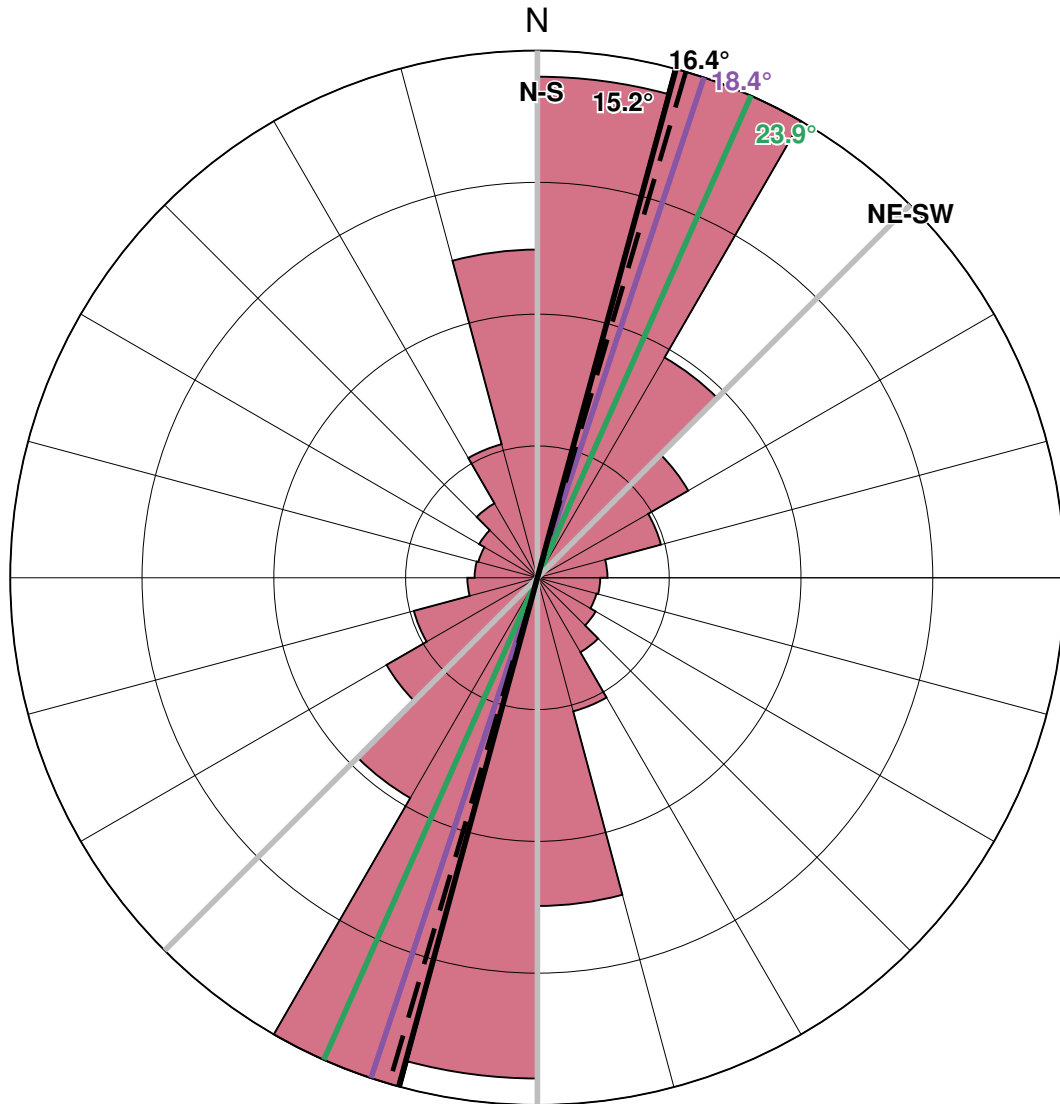


Figure 4. Circular histogram of all fast orientation measurements as denoted by pink shading. Lines are used to show the average strikes of the cross-cutting, conjugate strike-slip faults (grey), the average strikes of surface features in the Askja and Kverkfjöll rift segments (purple and green, respectively), the direction normal to spreading (dashed black), and the overall average orientation of the fast axis of anisotropy (black). There is a very strong correlation between the fast orientation direction and the direction normal to spreading, suggesting that stress is the dominant control on anisotropy.

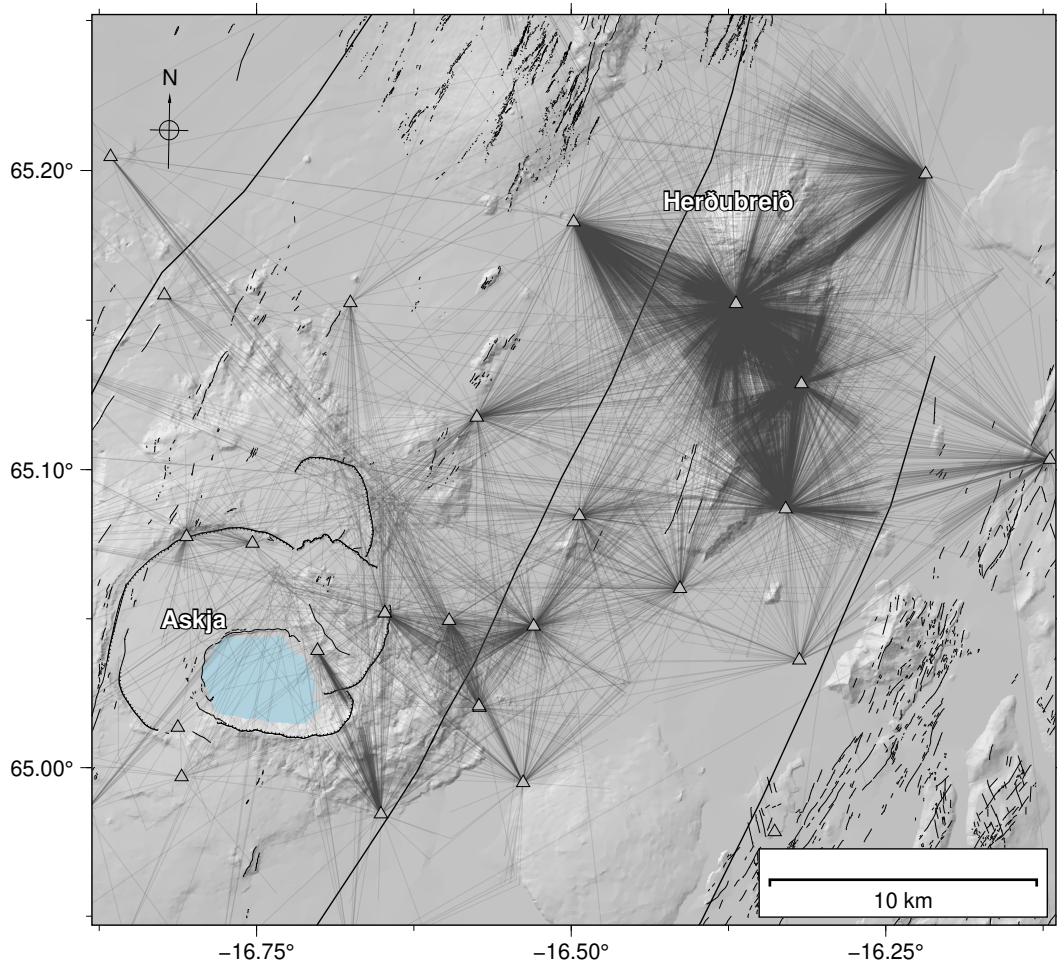


Figure 5. Map showing the raypath coverage for the study region. There is very good coverage around Askja and in the inter-rift segment around Herðubreið. The black lines depicting the raypaths are plotted at 85% transparency.

273 from other independent measures, such as ambient noise dispersion curves (Volk et al.,
 274 2021), response to seasonal changes in load in dv/v (Donaldson et al., 2019), and gen-
 275 eral profiles of pore space as a function of depth in oceanic crust (e.g. Carlson & Her-
 276 rick, 1990). While there is an element of bias in assigning the splitting observation to
 277 a single point in space, we follow precedent and use the mid-point of the raypath (Fig-
 278 ure 5) between the source and receiver before re-gridding the data. For near-vertical ray-
 279 paths, as is the case for the majority of our dataset due to the shear-wave window con-
 280 straint, this introduces negligible systematic error in the pattern of lateral variations. The
 281 application of a symmetric 2-D Gaussian spatial filter to the re-gridded observations fur-
 282 ther reduces the impact of this assumption on the observed lateral patterns. Here we present
 283 the results for a grid with 0.5 x 0.5 km cells and a minimum observation count of 10, and
 284 2-D Gaussian spatial filter with a half-width of 1 km (Figure 6). The key features of the
 285 lateral variation in anisotropy strength are robust to perturbations to both the grid pa-
 286 rameters and the smoothing radius. We trialed cell sizes varying from 0.25 x 0.25 km²
 287 – 1 x 1 km², minimum number of observations per bin between 3 and 15, and a smooth-
 288 ing radius of 1–3 km, and found that the results did not vary significantly (see suppl-
 289 ementary Figure S1). We acknowledge that the process of re-gridding the data in this way
 290 means that some azimuthal information is lost, but we deem it acceptable for the pur-
 291 pose of identifying trends in the strength of anisotropy across the rift segment. We mea-
 292 sure an anisotropic strength of $\sim 5\%$, with values ranging between 2–12 %, which spans
 293 the appropriate range expected for mechanisms proposed for elastic anisotropy of the
 294 crust.

295 **3.2.2 Fast axis orientation**

296 We re-grid the observations of ϕ by grouping them laterally by the midpoint along
 297 the event-receiver raypath (Figure 5), with the results presented in Figure 7. We use an
 298 adaptive quad-tree gridding method, which allows us to increase the detail (down to a
 299 minimum cell size of 2 x 2 km²) where we have a higher density of observations. The min-
 300 imum cell size used is on the same order as the uncertainties in the epicentral locations
 301 for the earthquakes in the catalog. Starting from a single cell spanning the entire study
 302 region, this process recursively subdivides a cell into four sub-cells if the number of ob-
 303 servations in the cell exceeds 200. Any cells with fewer than 50 observations are omit-
 304 ted from the final grid. Within each cell, the resultant vector is evaluated from which
 305 both the average orientation and the *mean resultant length*, \hat{R} , is determined. \hat{R} is a mea-
 306 sure of dispersion analogous to the variance (in the opposite sense) - values close to 0
 307 imply near uniform dispersion, whereas values close to 1 suggest that the orientations
 308 are tightly bunched around a particular value (e.g. Davis & Sampson, 1973). This al-

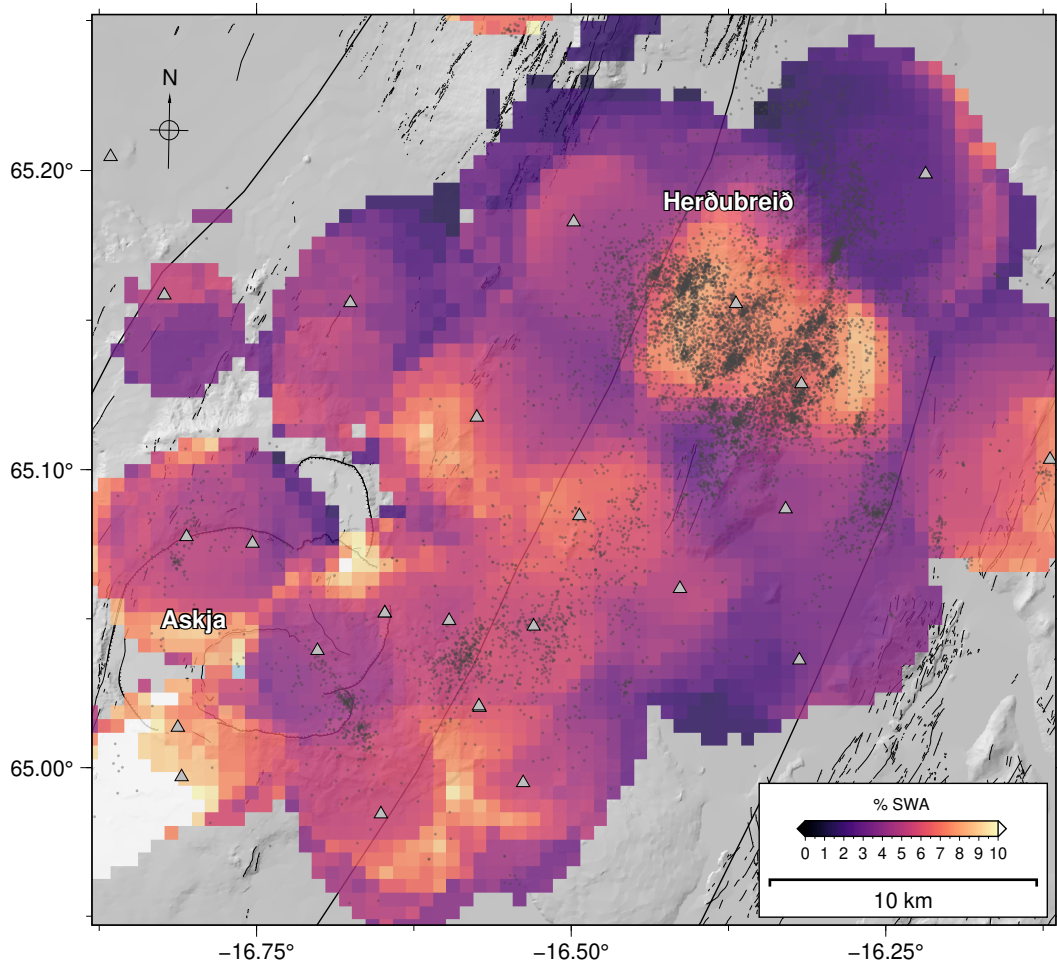


Figure 6. Map of the lateral variation in percentage shear wave anisotropy from earthquakes shallower than 10 km (denoted by the small black dots). Stations from which data have been used are denoted by the grey triangles.

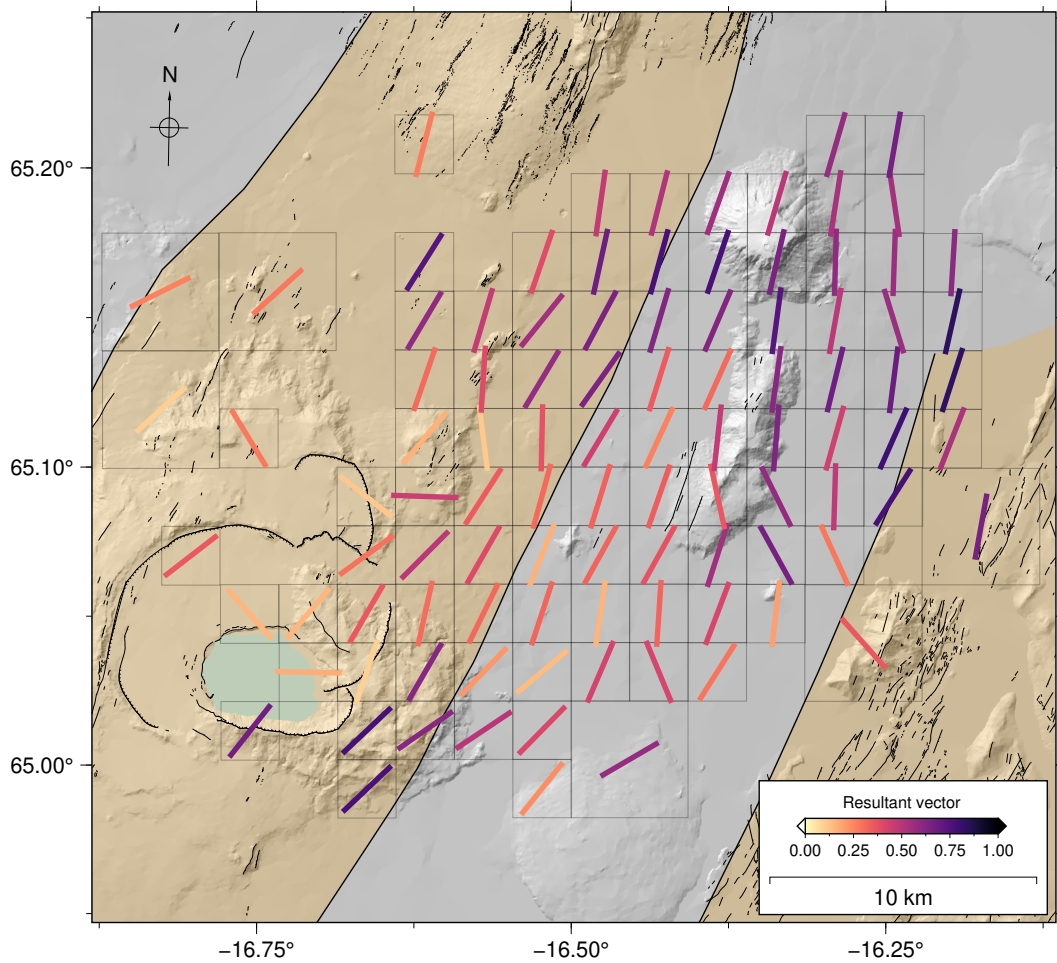


Figure 7. Lateral variations in observed fast axis orientations, ϕ . The observations have been assigned to the midpoint between source and receiver, then re-gridded using a quadtree method. The resultant grid is plotted using faint black lines. Within each cell, the bar represents the average fast orientation, colored by the ‘resultant vector’ which is a measure of dispersion/coherence of the orientation data. Darker colors indicate stronger coherence.

309 lows us to observe trends in the orientation of anisotropy, without constraining the source
 310 of anisotropy to be in the vicinity of the source or the receiver.

311 4 Discussion

312 4.1 Anisotropy orientation and strength

313 Our analysis of shear-wave splitting from earthquakes in the brittle, upper 10 km
 314 of crust around Askja has constrained the primary source of anisotropy to be in the top
 315 3–4 km of crust. The dominant orientation of the fast axis of anisotropy is strongly cor-

316 related with the strike of the rift (Figure 4). Together, these two observations provide
 317 compelling evidence for extensional stress as the underlying mechanism generating the
 318 anisotropy. This is consistent with other studies of local shear-wave splitting in similar
 319 environments, such as the East African Rift (Keir et al., 2005; Nowacki et al., 2018; Illsley-
 320 Kemp et al., 2017, 2019). The average delay times of shear-wave splitting observations
 321 ($\delta t = 0.10 \pm 0.08s$) is also consistent with these studies.

322 Although we attribute our observations of shear wave anisotropy to fractures or
 323 cracks in the shallow crust, there are other causes of anisotropy that may be a factor.
 324 For instance, aligned melt pockets could produce a signature of effective anisotropy with
 325 ridge-parallel orientation of the fast axis, as has been suggested in the upper mantle and
 326 lower crust of the Main Ethiopian Rift (Kendall et al., 2005; Hammond et al., 2014). How-
 327 ever, there is no evidence of this in the shallow crust beneath the NVZ, and ambient noise
 328 studies that constrain azimuthal variations of radial anisotropy are not consistent with
 329 such a mechanism (Volk et al., 2021). Furthermore, it would be unusual for melt pock-
 330 ets to focus in the very shallow crust, and be absent at greater depth, which would need
 331 to be the case to explain the trend shown in Figure 3. Another possibility is LPO as-
 332 sociated with deformation, lava flows or depositional processes. Recent measurements
 333 of radial anisotropy from ambient seismic noise (Volk et al., 2021) support the presence
 334 of LPO in the crust resulting from internal deformation or flow, but this appears to be
 335 largely restricted to depths below about 15 km, and therefore is unlikely to influence our
 336 results. Lava flows can align minerals such as plagioclase and clinopyroxene (Boiron et
 337 al., 2013), but this tends to occur at very short scale lengths horizontally and in depth,
 338 and consequently are unlikely to substantially contribute to our pattern of anisotropy
 339 over what is a relatively large study area.

340 When interpreting the map of SWA (Figure 6), we recommend that a greater im-
 341 portance be placed on the relative values, as opposed to the absolute values, which can
 342 be ‘tuned’ by varying the thickness chosen for the anisotropic layer. We primarily see
 343 elevated values of SWA in regions with elevated rates of seismicity, which is consistent
 344 with the idea that stress is the primary control on the mechanism generating anisotropy.

345 There is a region of elevated SWA to the south of Herðubreið (Figure 6), which cor-
 346 responds with a region of elevated seismic activity. A network of faults connects the Askja
 347 and Kverkfjöll rift segments, which are thought to accommodate the relative rates of plate-
 348 spreading. As such, it is reasonable to assume that this section of crust is heavily frac-
 349 tured and highly stressed, two conditions under which one would expect to see a higher
 350 anisotropic signal. This may also be an artefact of the assumption that the anisotropic
 351 layer has a uniform thickness across the region, though there is little evidence to vali-

352 date this from the individual 1-D station profiles. The relative low in SWA to the north-
353 east of Herðubreið corresponds to a region of elevated V_p/V_s observed in a tomographic
354 study of the region (Greenfield et al., 2016), which was interpreted to be a sign of ele-
355 vated fluid content. This is consistent with the suggestion from Nowacki et al. (2018)
356 that a higher V_p/V_s may indicate that there are more fluids present, which in turn causes
357 lower effective anisotropy, and may also explain the relatively low SWA below the Askja
358 geothermal field, on the eastern edge of the Öskjuvatn caldera. However, we should note
359 that elevated V_p/V_s need not necessarily imply lower anisotropy; for instance, Wang et
360 al. (2012) made laboratory observations of cracked samples and carried out effective me-
361 dia modeling, which suggested that the presence of high V_p/V_s ratios is indicative of sig-
362 nificant crack-induced anisotropy.

363 The spatial trends in the orientation of the fast axis of anisotropy was shown to
364 be broadly consistent with both the observed surface features from geological mapping
365 and the plate spreading direction (Figure 4). This is consistent with findings from other
366 rift environments (Menke et al., 1994; Illsley-Kemp et al., 2017; Nowacki et al., 2018),
367 where the fast axis of anisotropy was found to be aligned to the present-day minimum
368 compressive stress i.e. rift parallel. In these studies, the source of anisotropy is attributed
369 to aligned cracks in the top 3–4 km of the crust. Such crack alignment in the very shal-
370 low crust is also present in other tectonic environments, including fold and thrust belts.
371 For example, de Lorenzo and Trabacce (2011) investigate local earthquake shear-wave split-
372 ting using data recorded in the central Appenines, and attribute anisotropy in the top
373 4–5 km of the crust to fault-parallel fluid-filled crack systems.

374 As Figure 6 illustrates, the orientations of the fast axis of anisotropy are not uni-
375 formly rift-parallel; for instance, in the very south they have a stronger easterly compo-
376 nent compared to those in the north. Likewise, around Aluto in the Ethiopian Rift, the
377 orientations become more scattered. It is likely that the regional stress field in the south
378 of our area is overprinted by the ongoing deformation that is taking place around Askja.
379 Subsidence of the main caldera has been ongoing since 1983 (de Zeeuw-van Daltsen et
380 al., 2012), possibly due to the cooling and contraction of an underlying magma body,
381 although recent micro-gravity increases may be due to magma flow into a shallow magma
382 chamber (de Zeeuw-van Daltsen et al., 2013). Such local stress changes and associated
383 deformation may be responsible for scattered horizontal velocity vectors measured by
384 GPS stations in the vicinity of Askja (Árnadóttir et al., 2009; Drouin et al., 2017); con-
385 sequently, the disruption to the pattern of anisotropy around Askja is perhaps not sur-
386 prising. In the next section, we use stress modeling to investigate this phenomenon fur-
387 ther.

388

4.2 Stress modeling

389

390

391

392

393

394

395

396

397

398

399

Numerous studies have concluded that the orientation of anisotropy in the crust is generally controlled by the regional stress field and/or the alignment of structures, such as fissures and faults (Johnson et al., 2011; Illsley-Kemp et al., 2018; Savage et al., 2010). Distinguishing between stress-induced and structural anisotropy in the Northern Volcanic Zone is made somewhat more complex by the fact that the regional stress field is also the primary control on the orientation of structural features. It is observed, however, that the system of faults between the Askja and Kverkfjöll rift segments (responsible for a large proportion of the tectonic seismicity in the region) is composed of conjugate strike-slip faults oblique to the strike of the plate margin (see Figure 1). This suggests that we can rule out fabric resulting from the damage zones around faults as a mechanism generating (significant) anisotropy, based on the regional averages.

400

401

402

403

404

405

406

407

408

409

410

411

412

413

414

415

416

417

418

419

420

421

422

We explored the role of stress in the generation of anisotropy by modeling the regional stress field around Askja using the Coulomb v3.3 software package (Toda et al., 2011). Whereas the ductile lower crust is able to deform by continuous creep under the extensional stresses, accretion and extension of the brittle upper crust is episodic in nature. Over time, elastic strain accumulates in the brittle crust, before being released over short, intense periods of diking and extensional faulting, as seen during the 2014–15 eruption of Bárðarbunga. The brittle-ductile boundary across the NVZ sits between 6–8 km depth (Soosalu et al., 2010). We model this process using a buried dislocation, which has previously been used to model plate boundary deformation in the rift zones of Iceland (Árnadóttir et al., 2006; LaFemina et al., 2005). This model assumes that spreading below the brittle-ductile boundary is constant and equal to the full-spreading rate, represented by an opening Okada dislocation (Okada, 1992) extending from the locking depth to infinite depth. The stress singularity at the upper edge of the buried dislocation is eliminated from the model by tapering the dislocation such that the opening gradient goes to 0 at the topmost edge (Heimisson & Segall, 2020). The spreading boundary is taken to pass through Askja, striking along the rift segment at 015°N. A small component of spreading is assigned to the Kverkfjöll rift segment, though it is debatable whether any active spreading is occurring in this region. However, this inclusion does not significantly impact the result of the modeling. The ongoing deflation beneath Askja is incorporated using the best-fitting (analytical) solution from forward modeling (Drouin et al., 2017) of GPS data. This results in a point Mogi source at 3.5 km depth beneath the Askja caldera (see Figure 8), with a volumetric change of 0.0013 km³ / year. While both of these models are highly simplified, neglecting visco-elasticity in particular, they

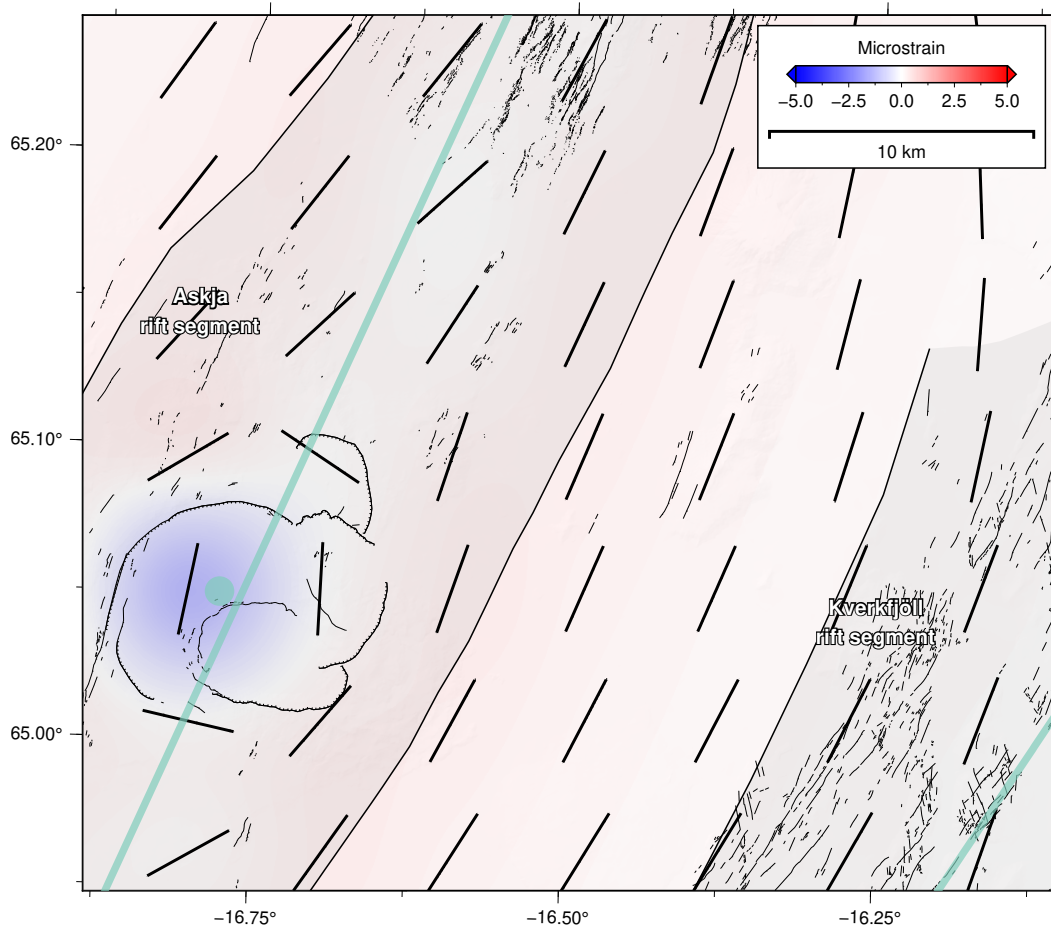


Figure 8. Modeled strain field at 0 km b.s.l. draped over a digital elevation model. Black bars represent the orientation of the maximum horizontal stress, S_{Hmax} . Blue bars delineate the modeled plate boundary segments. The blue circle denotes the centre of the observed deflation beneath Askja volcano.

423 are sufficient to capture, to first-order, the tectonic stress state of the crust. The input
 424 files for this modeling are available in the supporting information.

425 Using the method of Lund and Townend (2007), we extract the maximum horizon-
 426 tal stress vectors (S_{Hmax}) from the final model at a depth of 0 km b.s.l., where we ex-
 427 pect the impact of the stress field to have the most significant effect on the opening/closure
 428 of cracks. We observe a strong correlation between the orientations of fast directions and
 429 S_{Hmax} across the region, including a similar rotation moving from south to north. This
 430 provides a strong link between the stress field and the anisotropy, as would be expected
 431 for the EDA mechanism. The differences, particularly at the southern end of the region,
 432 are likely to be due to the component of strain imparted by the presence of the Vatna-

433 jökull ice cap, which is not included in the modeling. Interpolating the strain field di-
434 rectly from the available GPS data may prove valuable in assessing how much of the ob-
435 served rotation is due to the unmodeled components. Around Askja, the modeled strain
436 field shows a similar level of scatter to what is observed in Figure 7, though there is no
437 particular coherency in alignment. This is likely to be due to the limited spatial reso-
438 lution of the splitting measurements, coupled with the simplifying assumptions made in
439 the stress modeling. Careful analysis of the temporal changes in the anisotropic signal
440 in response to stress transients, such as the 2014 Bárðarbunga-Holuhraun dike intrusion,
441 may provide more supporting evidence for the EDA mechanism dominating the gener-
442 ation of anisotropy in the upper crust in the Northern Volcanic Zone.

443 5 Conclusions

444 We have presented shear-wave splitting results from the Northern Volcanic Zone,
445 Iceland, based on a large dataset of local earthquakes that span a period of over 7 years.
446 The dense, stable network has allowed us to image the anisotropic properties of the Ice-
447 landic crust with a high spatial resolution. These observations have allowed us to inves-
448 tigate the likely mechanisms generating this anisotropy, whether controlled by the stress
449 state or structural features in the crust. The main findings of the study include (i) based
450 on earthquakes that occur between the surface and 10 km depth, anisotropy is largely
451 restricted to the top 3–4 km of the crust; (ii) delay time variations in the shallow anisotropic
452 layer are consistent with the presence of cracks that gradually close with depth; (iii) SWA
453 is strongest in regions of elevated seismicity, particularly in the zone between the Askja
454 and Kverkfjöll rift segments, which appears to be heavily fractured; (iv) the dominant
455 orientation of the fast axis of anisotropy is almost perpendicular to the spreading direc-
456 tion, which indicates that regional stress is the dominant control on anisotropy; and (v)
457 in the neighbourhood of Askja, the orientation of the fast axis of anisotropy becomes scat-
458 tered, which is consistent with stress modeling results that use a Mogi source located 3.5
459 km beneath the main caldera. Future work will focus on the very deep earthquakes be-
460 neath the Northern Volcanic Zone, and the constraints they may be able to supply on
461 anisotropy in the lower crust, which has previously been imaged by ambient noise to-
462 mography.

463 Acknowledgments

464 The author contributions are as follows: **C.A.B.:** Conceptualization, Methodology, Soft-
465 ware, Formal Analysis, Visualization, Writing - Original Draft; **J.J.:** Supervision, Writ-

466 ing - Review & Editing; **R.S.W.:** Supervision, Funding acquisition, Writing- Review &
 467 Editing; **N.R.:** Supervision, Funding acquisition, Writing - Review & Editing.

468 A number of seismometers were borrowed from the Natural Environmental Research
 469 Council (NERC) SEIS-UK facility (loans 857, 914, 968, 980, 1022 and 1115). All wave-
 470 form data, except that recorded at the IMO station MKO, are available for download
 471 from the IRIS DMC. We thank the many people who participated in seismic data col-
 472 lection fieldwork in Iceland over the years, in particular Bryndís Brandsdóttir and Svein-
 473 björn Steinþórsson, without whom this work would not be possible. We also thank the
 474 Iceland Meteorological Office (IMO) for kindly providing the additional data from MKO.
 475 We especially thank Tim Greenfield and Tom Winder for their considerable efforts in pro-
 476 ducing the earthquake catalog that made this study possible. The shear-wave splitting
 477 measurements and Coulomb stress modeling input file can be downloaded from

478 <https://doi.org/10.5281/zenodo.5007022>. Data analysis was carried out using Python,
 479 with the following packages proving particularly useful: ObsPy (Beyreuther et al., 2010);
 480 SciPy (Virtanen et al., 2020); NumPy (Harris et al., 2020); Pandas (pandas development
 481 team, 2021). Data visualizations were performed using Matplotlib (Hunter, 2007) and
 482 Generic Mapping Tools (Wessel et al., 2019).

483 References

- 484 Allen, R. M. (2002). Plume-driven plumbing and crustal formation in Iceland. *Jour-*
 485 *nal of Geophysical Research*, *107*(B8). doi: 10.1029/2001jb000584
- 486 Árnadóttir, T., Jiang, W., Feigl, K. L., Geirsson, H., & Sturkell, E. (2006). Kine-
 487 matic models of plate boundary deformation in southwest Iceland derived from
 488 GPS observations. *Journal of Geophysical Research: Solid Earth*, *111*(B7).
 489 doi: 10.1029/2005JB003907
- 490 Árnadóttir, T., Lund, B., Jiang, W., Geirsson, H., Björnsson, H., Einarsson, P., &
 491 Sigurdsson, T. (2009). Glacial rebound and plate spreading: results from the
 492 first countrywide GPS observations in Iceland. *Geophysical Journal Interna-*
 493 *tional*, *177*(2), 691–716. doi: 10.1111/j.1365-246X.2008.04059.x
- 494 Athy, L. F. (1930). Density, porosity, and compaction of sedimentary rocks. *Amer-*
 495 *ican Association of Petroleum Geologists Bulletin*, *14*(1), 1–24. doi: 10.1306/
 496 3D93289E-16B1-11D7-8645000102C1865D
- 497 Audet, D., & McConnell, J. (1992). Forward modelling of porosity and pore pressure
 498 evolution in sedimentary basins. *Basin Research*, *4*(2), 147–162. doi: 10.1111/
 499 j.1365-2117.1992.tb00137.x
- 500 Backus, G. E. (1962). Long-wave elastic anisotropy produced by horizontal lay-

- 501 ering. *Journal of Geophysical Research*, 67(11), 4427–4440. doi: 10.1029/
502 jz067i011p04427
- 503 Baird, A. F., Kendall, J.-M., Sparks, R. S. J., & Baptie, B. (2015). Transtensional
504 deformation of Montserrat revealed by shear wave splitting. *Earth and Plane-*
505 *tary Science Letters*, 425, 179–186.
- 506 Bastow, I. D., Pilidou, S., Kendall, J. M., & Stuart, G. W. (2010). Melt-
507 induced seismic anisotropy and magma assisted rifting in Ethiopia: Evidence
508 from surface waves. *Geochemistry, Geophysics, Geosystems*, 11(6). doi:
509 10.1029/2010GC003036
- 510 Beyreuther, M., Barsch, R., Krischer, L., Megies, T., Behr, Y., & Wassermann, J.
511 (2010). ObsPy: A Python toolbox for seismology. *Seismological Research*
512 *Letters*, 81(3), 530–533.
- 513 Boiron, T., Bascou, J., Camps, P., Ferré, E., Maurice, C., Guy, B., . . . Launeau, P.
514 (2013). Internal structure of basalt flows: insights from magnetic and crystallo-
515 graphic fabrics of the La Palisse volcanics, French Massif Central. *Geophysical*
516 *Journal International*, 193(2), 585–602. doi: 10.1093/gji/ggs115
- 517 Boness, N. L., & Zoback, M. D. (2006). Mapping stress and structurally controlled
518 crustal shear velocity anisotropy in California. *Geology*, 34(10). doi: 10.1130/
519 G22309.1
- 520 Carlson, R. L., & Herrick, C. N. (1990). Densities and porosities in the oceanic crust
521 and their variations with depth and age. *Journal of Geophysical Research*,
522 95(B6), 9153–9170. doi: 10.1029/JB095iB06p09153
- 523 Christensen, N. I. (1984). Pore pressure and oceanic crustal seismic structure. *Geo-*
524 *physical Journal International*, 79(2), 411–423. doi: 10.1111/j.1365-246X.1984
525 .tb02232.x
- 526 Crampin, S. (1984). An introduction to wave propagation in anisotropic media.
527 *Geophysical Journal of the Royal Astronomical Society*, 76(1), 17–28. doi: 10
528 .1111/j.1365-246X.1984.tb05018.x
- 529 Crampin, S. (1994). The fracture criticality of crustal rocks. *Geophysical Journal In-*
530 *ternational*, 118(2), 428–438. doi: 10.1111/j.1365-246X.1994.tb03974.x
- 531 Darbyshire, F. A., White, R. S., & Priestley, K. F. (2000). Structure of the
532 crust and uppermost mantle of Iceland from a combined seismic and grav-
533 ity study. *Earth and Planetary Science Letters*, 181(3), 409–428. doi:
534 10.1016/S0012-821X(00)00206-5
- 535 Davis, J. C., & Sampson, R. J. (1973). *Statistics and data analysis in geology*
536 (Vol. 646). Wiley New York.
- 537 de Lorenzo, S., & Trabace, M. (2011). Seismic anisotropy of the shallow crust in

- 538 the Umbria–Marche (Italy) region. *Physics of the Earth and Planetary Interi-*
539 *ors*, 189(1-2), 34–46. doi: 10.1016/j.pepi.2011.09.008
- 540 de Zeeuw-van Dalssen, E., Pedersen, R., Hooper, A., & Sigmundsson, F. (2012).
541 Subsidence of Askja caldera 2000-2009: Modelling of deformation processes
542 at an extensional plate boundary, constrained by time series InSAR analy-
543 sis. *Journal of Volcanology and Geothermal Research*, 213-214, 72–82. doi:
544 10.1016/j.jvolgeores.2011.11.004
- 545 de Zeeuw-van Dalssen, E., Rymer, H., Sturkell, E., Pedersen, R., Hooper, A., Sig-
546 mundsson, F., & Ófeigsson, B. (2013). Geodetic data shed light on ongoing
547 caldera subsidence at Askja, Iceland. *Bulletin of volcanology*, 75(5), 1–13. doi:
548 10.1007/s00445-013-0709-2
- 549 Donaldson, C., Winder, T., Caudron, C., & White, R. S. (2019). Crustal seis-
550 mic velocity responds to a magmatic intrusion and seasonal loading in Ice-
551 land’s Northern Volcanic Zone. *Science Advances*, 5(11), eaax6642. doi:
552 10.1126/sciadv.aax6642
- 553 Drew, J., White, R. S., Tilmann, F., & Tarasewicz, J. (2013). Coalescence microseis-
554 mic mapping. *Geophysical Journal International*, 195(3), 1773–1785. doi: 10
555 .1093/gji/ggt331
- 556 Drouin, V., Sigmundsson, F., Ófeigsson, B. G., Hreinsdóttir, S., Sturkell, E., &
557 Einarsson, P. (2017). Deformation in the Northern Volcanic Zone of Iceland
558 2008–2014: An interplay of tectonic, magmatic, and glacial isostatic deforma-
559 tion. *Journal of Geophysical Research: Solid Earth*, 122(4), 3158–3178. doi:
560 10.1002/2016JB013206
- 561 Einarsson, P. (1991). Earthquakes and present-day tectonism in Iceland. *Tectono-*
562 *physics*, 189(1-4), 261–279. doi: 10.1016/0040-1951(91)90501-I
- 563 Garcia, S., Arnaud, N. O., Angelier, J., Bergerat, F., & Homberg, C. (2003). Rift
564 jump process in Northern Iceland since 10 Ma from $^{40}\text{Ar}/^{39}\text{Ar}$ geochronol-
565 ogy. *Earth and Planetary Science Letters*, 214(3-4), 529–544. doi:
566 10.1016/S0012-821X(03)00400-X
- 567 Graettinger, A. H., McGarvie, D. W., Skilling, I. P., Höskuldsson, A. H., &
568 Strand, K. (2019). Ice-confined construction of a large basaltic vol-
569 cano—Austurfjöll massif, Askja, Iceland. *Bulletin of Volcanology*, 81(2).
570 doi: 10.1007/s00445-019-1269-x
- 571 Green, R. G., White, R. S., & Greenfield, T. (2014). Motion in the north Iceland
572 volcanic rift zone accommodated by bookshelf faulting. *Nature Geoscience*,
573 7(1), 29–33. doi: 10.1038/ngeo2012
- 574 Greenfield, T., White, R. S., & Roecker, S. (2016). The magmatic plumbing system

- 575 of the Askja central volcano, Iceland, as imaged by seismic tomography. *Jour-*
 576 *nal of Geophysical Research: Solid Earth*, *121*(10), 7211–7229. doi: 10.1002/
 577 2016JB013163
- 578 Greenfield, T., White, R. S., Winder, T., & Ágústsdóttir, T. (2018). Seismicity of
 579 the Askja and Bárðarbunga volcanic systems of Iceland, 2009–2015. *Journal of*
 580 *Volcanology and Geothermal Research*, *391*. doi: 10.1016/j.jvolgeores.2018.08
 581 .010
- 582 Hammond, J. O., Kendall, J.-M., Wookey, J., Stuart, G., Keir, D., & Ayele, A.
 583 (2014). Differentiating flow, melt, or fossil seismic anisotropy beneath
 584 Ethiopia. *Geochemistry, Geophysics, Geosystems*, *15*(5), 1878–1894. doi:
 585 10.1002/2013GC005185
- 586 Han, S.-C., Schmerr, N., Neumann, G., & Holmes, S. (2014). Global characteristics
 587 of porosity and density stratification within the lunar crust from GRAIL grav-
 588 ity and Lunar Orbiter Laser Altimeter topography data. *Geophysical Research*
 589 *Letters*, *41*(6), 1882–1889. doi: 10.1002/2014GL059378
- 590 Harris, C. R., Millman, K. J., van der Walt, S. J., Gommers, R., Virtanen, P., Cour-
 591 napeau, D., ... others (2020). Array programming with NumPy. *Nature*,
 592 *585*(7825), 357–362.
- 593 Heimisson, E. R., & Segall, P. (2020). Physically Consistent Modeling of Dike-
 594 Induced Deformation and Seismicity: Application to the 2014 Bárðarbunga
 595 Dike, Iceland. *Journal of Geophysical Research: Solid Earth*, *125*(2), 1–21. doi:
 596 10.1029/2019JB018141
- 597 Hjartardóttir, A. R., Einarsson, P., Magnúsdóttir, S., Björnsdóttir, T., & Brandsdót-
 598 tir, B. (2016). Fracture systems of the Northern Volcanic Rift Zone, Iceland:
 599 An onshore part of the Mid-Atlantic plate boundary. In *Geological society*
 600 *special publication*. doi: 10.1144/SP420.1
- 601 Holtzman, B. K., Kohlstedt, D. L., Zimmerman, M. E., Heidelbach, F., Hiraga, T.,
 602 & Hustoft, J. (2003). Melt segregation and strain partitioning: Implications
 603 for seismic anisotropy and mantle flow. *Science*, *301*(5637), 1227–1230. doi:
 604 10.1126/science.1087132
- 605 Hunter, J. D. (2007). Matplotlib: A 2D graphics environment. *Computing in Science*
 606 *& Engineering*, *9*(3), 90–95. doi: 10.1109/MCSE.2007.55
- 607 Illsley-Kemp, F., Greenfield, T., & Keir, D. (2018). Seismic Anisotropy Reveals
 608 a Dynamic Link Between Adjacent Magmatic Segments Prior to Dyke Intru-
 609 sion. *Journal of Geophysical Research: Solid Earth*, *123*(11), 9800–9816. doi:
 610 10.1029/2018JB016420
- 611 Illsley-Kemp, F., Savage, M. K., Keir, D., Hirschberg, H. P., Bull, J. M., Gernon,

- 612 T. M., ... Goitom, B. (2017). Extension and stress during continental
613 breakup: Seismic anisotropy of the crust in Northern Afar. *Earth and Plane-*
614 *tary Science Letters*, *477*, 41–51.
- 615 Illsley-Kemp, F., Savage, M. K., Wilson, C. J., & Bannister, S. (2019). Mapping
616 stress and structure from subducting slab to magmatic rift: crustal seismic
617 anisotropy of the North Island, New Zealand. *Geochemistry, Geophysics,*
618 *Geosystems*, *20*(11), 5038–5056.
- 619 Johnson, J. H., Savage, M. K., & Townend, J. (2011). Distinguishing between
620 stress-induced and structural anisotropy at Mount Ruapehu volcano, New
621 Zealand. *Journal of Geophysical Research: Solid Earth*, *116*(12), 1–18. doi:
622 10.1029/2011JB008308
- 623 Keir, D., Kendall, J. M., Ebinger, C. J., & Stuart, G. W. (2005). Variations in
624 late syn-rift melt alignment inferred from shear-wave splitting in crustal earth-
625 quakes beneath the Ethiopian rift. *Geophysical Research Letters*, *32*(23), 1–4.
626 doi: 10.1029/2005GL024150
- 627 Kendall, J.-M., Stuart, G., Ebinger, C., Bastow, I., & Keir, D. (2005). Magma-
628 assisted rifting in Ethiopia. *Nature*, *433*(7022), 146–148. doi: 10.1038/
629 nature03161
- 630 LaFemina, P. C., Dixon, T. H., Malservisi, R., Árnadóttir, T., Sturkell, E., Sig-
631 mundsson, F., & Einarsson, P. (2005). Geodetic GPS measurements in
632 south Iceland: Strain accumulation and partitioning in a propagating ridge
633 system. *Journal of Geophysical Research: Solid Earth*, *110*(B11). doi:
634 10.1029/2005JB003675
- 635 Lesage, P., Heap, M. J., & Kushnir, A. (2018). A generic model for the shallow ve-
636 locity structure of volcanoes. *Journal of Volcanology and Geothermal Research*,
637 *356*, 114–126.
- 638 Lomax, A., Virieux, J., Volant, P., & Berge-Thierry, C. (2000). Probabilistic Earth-
639 quake Location in 3D and Layered Models.. doi: 10.1007/978-94-015-9536-0
640 _5
- 641 Lund, B., & Townend, J. (2007). Calculating horizontal stress orientations with full
642 or partial knowledge of the tectonic stress tensor. *Geophysical Journal Interna-*
643 *tional*, *170*(3), 1328–1335.
- 644 MacLennan, J., Mckenzie, D., & Gronvold, K. (2001). Plume-driven upwelling under
645 Central Iceland. *Earth and Planetary Science Letters*, *194*(1-2), 67–82. doi: 10
646 .1016/S0012-821X(01)00553-2
- 647 Martens, H. R., & White, R. S. (2013). Triggering of microearthquakes in Iceland
648 by volatiles released from a dyke intrusion. *Geophysical Journal International*,

- 649 194(3), 1738–1754. doi: 10.1093/gji/ggt184
- 650 Menke, W., Brandsdottir, B., Jakobsdottir, S., & Stefansson, R. (1994). Seismic
651 anisotropy in the crust at the mid-Atlantic plate boundary in south-west Ice-
652 land. *Geophysical Journal International*, 119(3), 783–790.
- 653 Mitchell, M. A., White, R. S., Roecker, S., & Greenfield, T. (2013). Tomographic
654 image of melt storage beneath Askja Volcano, Iceland using local microseismic-
655 ity. *Geophysical Research Letters*, 40(19), 5040–5046. doi: 10.1002/grl.50899
- 656 Nowacki, A., Wilks, M., Kendall, J. M., Biggs, J., & Ayele, A. (2018). Characteris-
657 ing hydrothermal fluid pathways beneath Aluto volcano, Main Ethiopian Rift,
658 using shear wave splitting. *Journal of Volcanology and Geothermal Research*,
659 356, 331–341. doi: 10.1016/j.jvolgeores.2018.03.023
- 660 Nuttli, O. (1961). The effect of the earth’s surface on the S wave particle motion.
661 *Bulletin of the Seismological Society of America*, 51(2), 237–246.
- 662 Okada, Y. (1992). Internal deformation due to shear and tensile faults in a half-
663 space. *Bulletin of the Seismological Society of America*, 82(2), 1018–1040.
- 664 Pagli, C., Sigmundsson, F., Árnadóttir, T., Einarsson, P., & Sturkell, E. (2006).
665 Deflation of the Askja volcanic system: Constraints on the deformation source
666 from combined inversion of satellite radar interferograms and GPS measure-
667 ments. *Journal of Volcanology and Geothermal Research*, 152(1-2), 97–108.
668 doi: 10.1016/j.jvolgeores.2005.09.014
- 669 pandas development team, T. (2021). *pandas-dev/pandas: Pandas 1.3.0rc1*. Zenodo.
670 doi: 10.5281/zenodo.4940217
- 671 Pedersen, R., Sigmundsson, F., & Masterlark, T. (2009). Rheologic controls on inter-
672 rifting deformation of the Northern Volcanic Zone, Iceland. *Earth and Plane-
673 tary Science Letters*, 281(1-2), 14–26. doi: 10.1016/j.epsl.2009.02.003
- 674 Savage, M. K., Wessel, A., Teanby, N. A., & Hurst, A. W. (2010). Automatic mea-
675 surement of shear wave splitting and applications to time varying anisotropy at
676 Mount Ruapehu volcano, New Zealand. *Journal of Geophysical Research: Solid
677 Earth*, 115(12), 1–17. doi: 10.1029/2010JB007722
- 678 Sigmundsson, F., Hooper, A., Hreinsdóttir, S., Vogfjörð, K. S., Ófeigsson, B. G.,
679 Heimisson, E. R., . . . Eibl, E. P. (2014). Segmented lateral dyke growth in a
680 rifting event at Bárðarbunga volcanic system, Iceland. *Nature*, 517(7533). doi:
681 10.1038/nature14111
- 682 Silver, P. G., & Chan, W. W. (1991). Shear wave splitting and subcontinental
683 mantle deformation. *Journal of Geophysical Research: Solid Earth*, 96(B10),
684 16429–16454. doi: 10.1029/91JB00899
- 685 Soosalu, H., Key, J., White, R. S., Knox, C., Einarsson, P., & Jakobsdóttir, S. S.

- 686 (2010). Lower-crustal earthquakes caused by magma movement beneath Askja
 687 volcano on the north Iceland rift. *Bulletin of Volcanology*, *72*(1), 55–62. doi:
 688 10.1007/s00445-009-0297-3
- 689 Sturkell, E., Sigmundsson, F., & Slunga, R. (2006). 1983–2003 decaying rate of
 690 deflation at Askja caldera: Pressure decrease in an extensive magma plumb-
 691 ing system at a spreading plate boundary. *Bulletin of Volcanology*, *68*(7-8),
 692 727–735. doi: 10.1007/s00445-005-0046-1
- 693 Teanby, N. A., Kendall, J. M., & van der Baan, M. (2004). Automation of shear-
 694 wave splitting measurements using cluster analysis. *Bulletin of the Seismologi-
 695 cal Society of America*, *94*(2), 453–463. doi: 10.1785/0120030123
- 696 Thomas, C., & Kendall, J. (2002). The lowermost mantle beneath northern
 697 Asia—II. Evidence for lower-mantle anisotropy. *Geophysical Journal Inter-
 698 national*, *151*(1), 296–308. doi: 10.1046/j.1365-246X.2002.01760.x
- 699 Toda, S., Stein, R., Sevilgen, V., & Lin, J. (2011). *Coulomb 3.3 Graphic-rich de-
 700 formation and stress-change software for earthquake, tectonic, and volcano
 701 research and teaching-user guide*. (Tech. Rep.).
- 702 Tryggvason, E. (1989). Ground deformation in Askja, Iceland: Its source and pos-
 703 sible relation to flow of the mantle plume. *Journal of Volcanology and Geother-
 704 mal Research*, *39*(1), 61–71. doi: 10.1016/0377-0273(89)90021-8
- 705 Virtanen, P., Gommers, R., Oliphant, T. E., Haberland, M., Reddy, T., Courn-
 706 peau, D., . . . others (2020). SciPy 1.0: fundamental algorithms for scientific
 707 computing in Python. *Nature methods*, *17*(3), 261–272.
- 708 Volk, O., White, R. S., Pilia, S., Green, R. G., MacLennan, J., & Rawlinson, N.
 709 (2021). Oceanic crustal flow in Iceland observed using seismic anisotropy.
 710 *Nature Geoscience*, *14*(3), 168–173. doi: 10.1038/s41561-021-00702-7
- 711 Walsh, E., Arnold, R., & Savage, M. K. (2013). Silver and Chan revisited. *Journal
 712 of Geophysical Research: Solid Earth*, *118*(10), 5500–5515. doi: 10.1002/jgrb
 713 .50386
- 714 Wang, X. Q., Schubnel, A., Fortin, J., David, E. C., Guéguen, Y., & Ge, H. K.
 715 (2012). High Vp/Vs ratio: Saturated cracks or anisotropy effects? *Geophysical
 716 Research Letters*, *39*(11), 2–7. doi: 10.1029/2012GL051742
- 717 Wessel, P., Luis, J., Uieda, L., Scharroo, R., Wobbe, F., Smith, W., & Tian, D.
 718 (2019). The Generic Mapping Tools version 6. *Geochemistry, Geophysics,
 719 Geosystems*, *20*(11), 5556–5564. doi: 10.1029/2019GC008515
- 720 White, R. S., & McKenzie, D. (1995). Mantle plumes and flood basalts. *Jour-
 721 nal of Geophysical Research: Solid Earth*, *100*(B9), 17543–17585. doi: 10.1029/
 722 95jb01585

723 Winder, T., White, R. S., Green, R. G., & Greenfield, T. (2018). A Surge in Seis-
724 micity in a Network of Cross-Cutting Conjugate Strike-Slip Faults Triggered
725 by the 2014 Bárðarbunga-Holuhraun Dike Intrusion. In *Agu fall meeting*
726 *abstracts* (Vol. 2018, pp. V23C-08).